Pixel scaling in infrared focal plane arrays

Peter B. Catrysse[1,*] and Torbjorn Skauli[1,2]

[1]Edward L. Ginzton Laboratory, Stanford University, Stanford, California 94305-4088, USA

[2]Norwegian Defence Research Establishment, P.O. Box 25, Kjeller 2027, Norway

*Corresponding author: pcatryss@stanford.edu

Received 2 January 2013; revised 22 January 2013; accepted 23 January 2013;
posted 23 January 2013 (Doc. ID 182331); published 18 February 2013

We discuss effects that arise in pixels of IR focal plane arrays (FPAs) when pixel size scales down to approach the wavelength of the incident radiation. To study these effects, we perform first-principles electromagnetic simulations of pixel structures based on a mercury–cadmium–telluride photoconductor for use in FPAs. Specifically, we calculate the pixel quantum efficiency and crosstalk as pixel size scales from 16 μm, which is in the range of current detectors, down to 0.75 μm, corresponding to subwavelength detectors. Our numerical results indicate the possibility of wavelength-size (~4 μm) and even subwavelength-size (~1 μm) pixels for IR FPAs. In addition, we explore opportunities that emerge for controlling light with subwavelength structures inside FPA pixels. As an illustration, we find that the low-pass filtering effect of a metal film aperture can exemplify the impact and the possible role that wavelength-scale optics plays in very small pixels.

OCIS codes: 040.3060, 050.6624, 110.0110, 110.3080.

1. Introduction

The current trend in focal plane arrays (FPAs) for IR imaging systems is toward smaller pixels. For fixed-FPA size, this enables larger pixel counts and increased spatial sampling. In turn, it can provide recorded images with improved spatial resolution if the imaging lens does not limit resolution. Pixel sizes in FPAs used in mid-wave IR (MWIR, 3–5 μm) and long-wave IR (LWIR, 8–12 μm) systems are being reduced below 20 μm, approaching the diffraction limit of conventional imaging optics. On the other hand, even a diffraction-limited pixel size is still relatively large compared with the feature sizes that can be achieved with state-of-the-art nanofabrication approaches. Thus, it is generally interesting to investigate pixel scaling beyond the diffraction limit, as well as to study opportunities for new functionalities in FPA pixels using wavelength- and, perhaps even, subwavelength-scale optics that are enabled by modern nanofabrication [1–4].

We note that a similar scaling trend has occurred for pixels in solid-state image sensors based on silicon photodetectors, where complementary metal–oxide–semiconductor (CMOS) technology has become the de facto standard for implementing image sensors for visible imaging applications. Although the scaling of CMOS technology can improve the performance of image sensors in a variety of ways [5], it primarily has been used to decrease pixel size and increase spatial resolution [5,6]. The scaling of image sensor pixels requires careful attention to light propagation within the pixel and has been analyzed with rigorous electromagnetic field simulations [7–11].

In this paper, we study the scaling of simple pixel structures for IR FPAs using first-principles electromagnetic simulation techniques and electronic device models that have been applied successfully in the design and analysis of CMOS image sensors. Using techniques from the field of nanophotonics, we also explore opportunities that emerge for controlling light with subwavelength optics in very small FPA pixels.

1559-128X/13/070C72-06$15.00/0

2. Models and Methods

In this section, we describe the model for the FPA pixel structure. It consists of a two-dimensional (2D) pixel cross section with associated geometry and material descriptions. We then identify quantum efficiency (QE) and crosstalk as performance metrics for the pixel study. Finally, we detail the first-principles electromagnetic simulation and pixel analysis procedures.

A. FPA Pixel Model

A prediction of FPA pixel performance requires a detailed understanding of the pixel properties. These are captured by using a physically accurate FPA pixel model. Such a model consists of both material descriptions and a description of the pixel structure geometry. The material descriptions can be in the form of materials models or be based on empirical measurement data obtained by a spectral characterization of the optical properties of the pixel materials.

With the notable exception of microbolometers, IR FPAs generally are fabricated from materials other than silicon, including narrow-gap semiconductors and intersubband-absorbing layered quantum structures. The photosensitive volume of an IR FPA pixel is normally a photodiode, but a photoconductive mode of operation often is used for linear or one-dimensional (1D) arrays and few-element detectors [12] as well as for quantum-well photodetectors [13]. An IR FPA pixel typically also includes a substrate, metallic contacts, and additional layers, such as passivation, antireflection coatings, or adhesives. A CMOS readout circuit normally is part of an IR FPA assembly, but outside the optical path that is of interest in this work.

As an example pixel structure, we consider an $Hg_{1-x}Cd_xTe$ (mercury–cadmium–telluride, MCT) photoconductive pixel shown in Fig. 1. A gold film is deposited on an MCT layer, patterned to form electrical contacts that also delineate the active area of the detector. The MCT layer is supported either by its epitaxy substrate or by a sapphire wafer as shown. The main application for this type of detector is in scanned linear arrays and single detector elements.

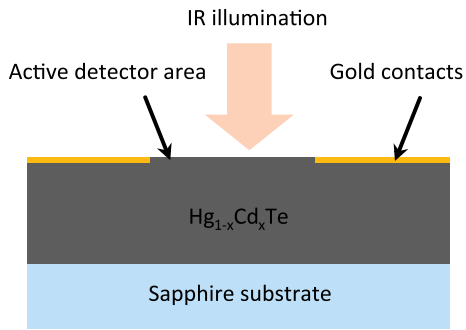

Fig. 1. $Hg_{1-x}Cd_xTe$ (MCT) photoconductive pixel for use in IR FPAs. Cross section of the pixel structure comprising an MCT layer with gold contacts on a sapphire substrate. The entire pixel structure typically measures 20–50 μm laterally and 4–10 μm vertically.

Although 2D detector arrays are commonly used, the photoconductive device is interesting for an exploratory study because it incorporates metal layers on the input side that may be patterned to form (sub) wavelength-scale optical structures and, at the same time, a photoconductor-based pixel may be more easily within reach for experiments. Moreover, the architecture is well adapted to cross-sectional simulation being essentially a 2D device.

This study considers pixels with a photoconductor width (distance between the gold contacts) ranging from 16 to 0.75 μm. This allows us to span a wide range of detectors, ranging from those found in current FPA pixels all the way to deep-subwavelength detectors. The photoconductor fills the areas between the electrical contacts, which are represented by a gold film of thickness 1 μm, but the MCT also extends below the gold contacts for a total thickness of 10 μm. This is representative of typical MCT layer thicknesses.

B. Performance Metrics: Pixel Quantum Efficiency and Pixel Crosstalk

To evaluate the pixel performance, we compute pixel QE and pixel crosstalk, starting from the simulated electromagnetic field patterns. Both of these measures have an optical and an electrical component. Pixel QE is defined as the product of optical efficiency and internal QE. The former is the fraction of optical power incident on the surface of each FPA pixel that reaches the intended photodetector [14]. The latter is the efficiency with which the FPA photodetector converts the incident photons into electrons, which then are collected to form an electrical signal. Pixel crosstalk is similarly defined as the product of two parts: the optical crosstalk—that is, the fraction of optical power incident on each FPA pixel that reaches the photodetectors in adjacent pixels [14]; and the fraction of the photons that subsequently is converted into electrons and collected by the neighboring pixel's detector.

C. Simulation Method

Analytical approximations based on ray optics often can be used to estimate the performance of photodetectors. When FPA pixels have a size comparable to the wavelength, however, first-principles methods for solving Maxwell's equations must be used to calculate the distribution of the electromagnetic fields inside the pixel. Here, we use a finite-difference frequency-domain (FDFD) approach in which the electromagnetic fields are calculated by solving a large sparse linear system derived from Maxwell's equations [15]. FDFD is a powerful tool, used in the field of nanophotonics, to explicitly determine the electric and magnetic fields at every point when electromagnetic radiation (light) is incident on an optical or optoelectronic structure.

The incident light is modeled as a plane-wave excitation in air just above the FPA pixel structure. This is representative of a uniform beam with a

lateral extent much larger than the pixel size. The FDFD calculations are performed at each frequency. Material properties are described by measured permittivities, thus directly taking into account material dispersion as well as loss without need for dispersive material models. The wavelength range of interest here, between 4 and 10 μm, is sampled about 80 times (linearly spaced in frequency). This is a good compromise between achieving good spectral resolution and maintaining a reasonable calculation time. For the spatial sampling of the simulation domain, we use a 10 nm grid in the vertical direction and a grid size between 30 and 800 nm in the horizontal direction, depending on the size of the simulation domain for different size pixels. The simulation domain is terminated with perfectly matched layers in the vertical direction and with periodic boundaries in the horizontal direction [16]. Conveniently for our use, the periodic boundaries can be interpreted as representing adjacent pixels in a FPA configuration (albeit in a direction orthogonal to the normal 1D array architecture).

As an example, Figs. 2(a) and 2(b) show the electric field profile inside the pixel cross section when illuminated by transverse electrically (TE) polarized light (electric field perpendicular to the pixel cross section) with wavelengths above and below the MCT bandgap cutoff. This polarization is relevant for pixel scaling, because the aperture size limits the wavelengths for which efficient light throughput is possible. Moreover, this allows us to make predictions for fully 3D pixels used in 2D FPAs as this effect also occurs for unpolarized light incident on pixels with finite size in two transverse dimensions. The MCT bandgap can be varied over a wide range by choosing the Cd mole fraction x. Here, we use tabulated material data for $Hg_{1-x}Cd_xTe$ with $x = 0.2$ and a bandgap corresponding to a cutoff wavelength of 7 μm at room temperature [17]. This ensures that wavelengths from well above to well below the bandgap fall within the spectral range of ambient thermal radiation. Adaptation to the atmospheric transmission spectrum would be necessary in most applications. Figures 2(a) and 2(b) show the magnitude of the electric field. Bright areas correspond to large field magnitudes and dark areas to small field magnitudes. The electric field profiles illustrate that incoming light is absorbed close to the detector surface for wavelengths well below bandgap cutoff, whereas light at wavelengths longer than the bandgap cutoff is transmitted through the MCT layer and into the substrate. Diffraction effects from the aperture (delineated by the gold contacts) are seen clearly in the field maps, already illustrating the utility of detailed field simulations.

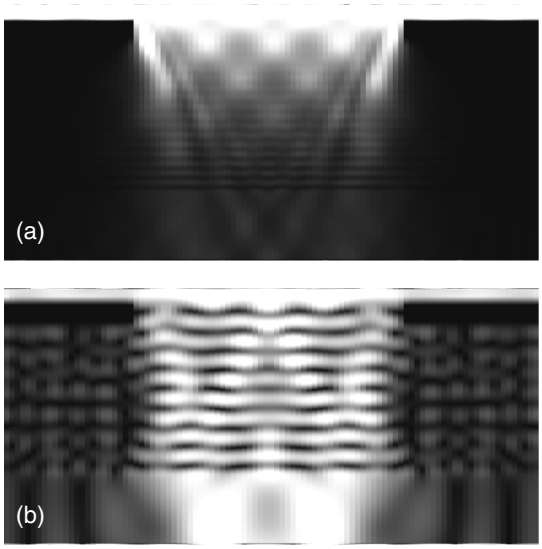

Fig. 2. Electric field profile inside an MCT photoconductive pixel (10 μm thick MCT layer, 16 μm wide detector, and 1 μm thick gold contacts). The fields are due to normally incident, transverse-electrically (TE) polarized radiation at a wavelength of (a) 4 μm and (b) 10 μm. Bright areas correspond to large field magnitudes and dark areas to small field magnitudes.

D. Quantum Efficiency and Crosstalk Calculation

We characterize the pixel performance by its QE and by the crosstalk to neighboring pixels. These quantities can be derived from the electric field maps and the electrical properties of the detector. Because the emphasis is on optical aspects, we do not use a detailed electrical model of a specific detector device. We consider quantum detectors without gain, where the QE is defined as the fraction of incoming photons that produce a photoelectron at the electrical output. Instead of a full electrical model for a particular device, we approximate the device behavior by assuming that the active volume is the region directly underneath the detector aperture, as illustrated in Fig. 3. All photons absorbed in this volume are assumed to generate a photoelectron, which also is collected. Thus, the QE estimates represent only optical losses resulting from absorption outside the defined active volume or transmission through the device. This is a reasonable approximation for a photoconductor in the high-bias "sweep-out" limit. The optical effects discussed here are present in other device architectures. In particular, charge collection efficiency is likely to be high for detectors with a very small active volume, regardless of whether it is electrically a photoconductor or a photodiode. For the photon rate, we take as reference the rate of photons arriving at the detector aperture.

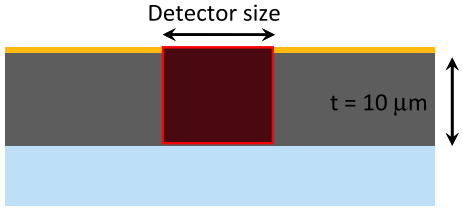

Fig. 3. QE model for an MCT photoconductive FPA pixel. QE is based on a simple device model where collection efficiency is assumed to be unity in the MCT volume below the active area of the detector, and zero elsewhere.

Under these assumptions, the QE is most readily expressed as a ratio of absorbed to incident optical power, starting from the simulated electromagnetic field patterns of a monochromatic wave. The incident power is obtained by integrating the component of the Poynting vector of the incoming wave, $\vec{S}_{\text{inc}}$, along the surface normal $\vec{n}$ over the detector area A_{det}:

$$P_{\text{inc}} = \iint_{A_{\text{det}}} \vec{S}_{\text{inc}} \cdot \vec{n} \, \mathrm{d}A = \frac{A_{\text{det}}}{Z_0} \sqrt{\varepsilon_{\text{inc}}} E_{\text{inc}}^2 \cos\theta, \quad (1)$$

where Z_0 is the impedance of free space and ε_{inc} is the relative permittivity of the incident medium, which is assumed to be nonmagnetic and nonabsorbing. E_{inc} is the electric field strength and θ is the angle of incidence of an incident plane wave.

In a classical electromagnetic sense, the absorbed power in the active detector volume, V_{det}, of the FPA pixel is the power dissipated by the field due to the detector material's conductivity σ, which is related to the complex dielectric constant ε by $\sigma = \omega \, \mathrm{Im}(\varepsilon)$. This gives

$$P_{\text{abs}} = \iiint_{V_{\text{det}}} \sigma E^2 \mathrm{d}V = \omega \varepsilon_0 \, \mathrm{Im}(\varepsilon_{\text{det}}) \iiint_{V_{\text{det}}} E^2 \mathrm{d}V, \quad (2)$$

where E is the spatially varying electric field taken from first-principles electromagnetic field simulations, ω is the angular frequency of the wave, and ε_{det} is the relative permittivity of the detector material (assumed to be homogeneous and nonmagnetic).

The pixel QE becomes

$$\eta = \frac{P_{\text{abs}}}{P_{\text{inc}}} = \frac{\omega \varepsilon_0 Z_0 \, \mathrm{Im}(\varepsilon_{\text{det}})}{\sqrt{\varepsilon_{\text{inc}}} A_{\text{det}}} \iiint_{V_{\text{det}}} \left(\frac{E}{E_{\text{inc}}} \right)^2 \mathrm{d}V, \quad (3)$$

where the integral is evaluated numerically from the simulated electric field pattern. As noted, Eq. (3) represents the optical QE and assumes a simplified electrical device model with ideal charge collection in the active volume.

Pixel crosstalk through the detector material can be estimated by a similar integration over a different volume taken to represent a neighboring pixel but covered by the gold layer, as shown in Fig. 5 and discussed in Section 3.B.

3. Results

This section describes the results of the QE and crosstalk calculations for photoconductive FPA pixels of varying pixel sizes subject to IR radiation between 4 and 10 μm (MWIR and LWIR).

A. Quantum Efficiency

Figure 4 shows the QE spectra for pixels with a detector width (between contacts) ranging from 16 μm, in the range of current FPA detectors, to 0.75 μm, corresponding to subwavelength-size detectors.

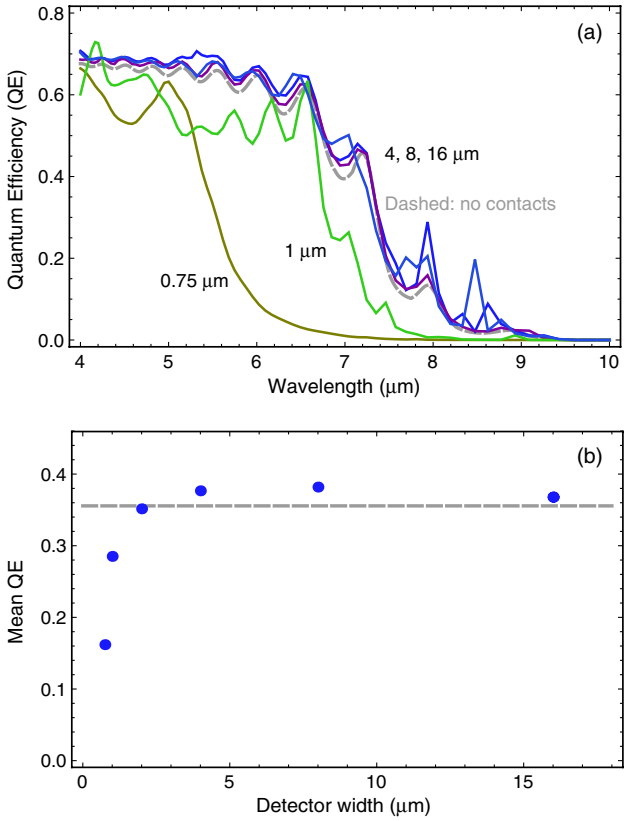

Fig. 4. QE for FPA pixels with a detector width (contact separation) ranging from 0.75 to 16 μm. (a) QE as a function of wavelength. The dashed gray curve, from an independent thin-film calculation, represents absorption in an MCT layer without gold contacts. (b) Mean QE over the wavelength range of 4–10 μm as a function of detector width. The dashed gray curve represents mean absorption in an MCT layer without gold contacts.

In Fig. 4(a), the QE is plotted versus wavelength across the MCT bandgap cutoff. For comparison, the spectrum of absorption by an MCT layer without gold contacts is shown as a dashed gray curve. It is obtained independently from an analytical 1D calculation based on a transfer matrix method for thin-film stratified media [18]. The spectrum coincides with the numerical FDFD simulation results for a wide range of (finite) detector sizes. We also observe peaks around 8 μm resulting from the periodic boundaries in the numerical results, which are representative of the FPA periodicity. The gold contacts do not significantly influence the spectral QE for devices as small as 4 μm (wavelength size). For detector widths smaller than 2 μm (subwavelength size), the spectral QE cuts off at shorter wavelengths. This is due to the short-pass spectral behavior of the aperture containing detector material between the metal contacts, which occurs when the fundamental propagating TE mode supported by the aperture goes into waveguide cutoff. For a 0.75 μm wide detector, the wavelength at which the spectral QE starts to cut off is dictated by the waveguide cutoff, which is about 2 μm shorter than the bandgap cutoff.

In Fig. 4(b), the mean QE over the 4–10 μm spectral range is shown as a function of detector width.

The mean QE is approximately constant for detector widths down to 4 μm and starts to fall off for widths smaller than 2 μm (transition from bandgap to waveguide cutoff). The QE results indicate the possibility of meaningfully shrinking IR FPA pixels down to the wavelength and even subwavelength scale (1–2 μm). The spectral filtering effected by the aperture containing detector material is a basic example of the possibility of implementing optical functions using metal layers in proximity to the active volume of a detector inside FPA pixels.

B. Crosstalk

Even if a subwavelength pixel could be made, crosstalk between FPA pixels could be a challenge. We consider the case in which neighboring pixels contain different filtering optics (e.g., for spectral or polarimetric imaging), so that crosstalk resulting from diffraction blur of the imaging optics is not a concern. With decreasing pixel size, however, the risk of crosstalk increases due to propagation of light within the detector structures. Electrical isolation, such as a gap (vacuum) between pixels, may prevent or limit crosstalk by diffusion of carriers, but it does not prevent optical crosstalk at these small scales because the extent of the evanescent fields is comparable to pixel pitch. In our simple architecture, optical crosstalk can be estimated by integrating the absorption in a volume corresponding to a neighboring pixel but covered under the gold layer. We assume for simplicity that the pixel pitch is twice the detector width. This volume is indicated in Fig. 5. Figure 6 shows the resulting crosstalk estimates for pixels with a detector width ranging from 0.75 to 16 μm. In Fig. 6(a), crosstalk is expressed as a spectral QE. In Fig. 6(b), crosstalk QE is averaged over wavelengths from 4 to 10 μm as a function of detector width.

For detector widths larger than 4 μm, the crosstalk occurs for long wavelengths because these are able to pass through the aperture and propagate relatively far laterally in the MCT layer due to their weak absorption in the detector material. For detector widths smaller than 1 μm, the wavelengths near the bandgap are filtered out by the aperture. The shorter wavelengths still propagate through the detector aperture and contribute to some crosstalk. The amount of crosstalk is moderate, however, remaining at a

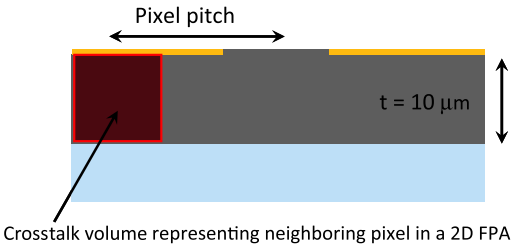

Fig. 5. Optical crosstalk model for an MCT photoconductive FPA pixel. Optical crosstalk can be estimated by integrating the absorption in a volume corresponding to a neighboring pixel, but covered under the gold layer. We assume for simplicity that the pixel pitch is twice the detector width.

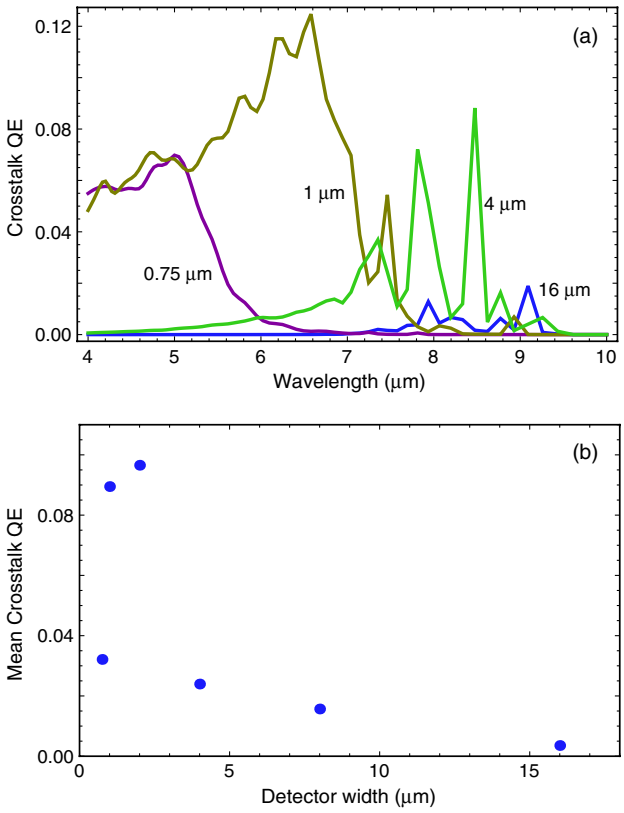

Fig. 6. Crosstalk for FPA pixels with a detector width ranging from 16 to 0.75 μm. The pixel pitch is taken to be twice the detector width. (a) Spectral crosstalk QE given as a function of wavelength, and (b) mean crosstalk QE over the wavelength range of 4–10 μm as a function of detector width.

manageable level of a few percent for detector widths that are 5–10 times smaller than the wavelength. The low levels of crosstalk are due to the strong absorption of the MCT material at photon energies well above the bandgap. Hence, our results constitute encouraging evidence for the possibility of using FPAs with subwavelength pixels provided that the absorption is sufficiently strong. For example, the results for the smallest pixel size in Fig. 4 indicate a responsivity cutoff suitable for detection in the atmospheric transmission band ~3–5 μm wavelength. Reducing the bandgap to achieve strong absorption may have the disadvantage of requiring a lower temperature of operation for the detector, but this may be offset by the large design space that would be opened by subwavelength detector elements.

4. Conclusion

This paper has illustrated challenges and possible opportunities that arise in IR FPAs when pixel size scales down to the single wavelength range. Using first-principles electromagnetic simulations of pixel structures based on an MCT photoconductor, we calculated the pixel QE and crosstalk as pixel size scales from 16 μm, in the range of current FPA detectors, down to 0.75 μm, corresponding to subwavelength detectors. Our simulation results indicate the possibility

of wavelength-size (~4 μm) and even subwavelength-size (~1 μm) pixels. The article also explored opportunities that emerge for controlling light with subwavelength optics in very small pixels. Here, the low-pass filtering effect of the aperture is a good example of the impact and possible role that wavelength-scale optics can play in very small pixels. Crosstalk between pixels in this case may be mitigated by using a strongly absorbing detector material.

This work was supported in part by a Defense Advanced Research Projects Agency (DARPA) grant (No. W911NF-12-1-0281).

References

1. Z. F. Yu, G. Veronis, S. H. Fan, and M. L. Brongersma, "Design of midinfrared photodetectors enhanced by surface plasmons on grating structures," Appl. Phys. Lett. **89**, 151116 (2006).
2. E. Laux, C. Genet, T. Skauli, and T. W. Ebbesen, "Plasmonic photon sorters for spectral and polarimetric imaging," Nat. Photonics **2**, 161–164 (2008).
3. L. Verslegers, P. B. Catrysse, Z. F. Yu, J. S. White, E. S. Barnard, M. L. Brongersma, and S. H. Fan, "Planar lenses based on nanoscale slit arrays in a metallic film," Nano Lett. **9**, 235–238 (2009).
4. C. A. Keasler and E. Bellotti, "A numerical study of broadband absorbers for visible to infrared detectors," Appl. Phys. Lett. **99**, 091109 (2011).
5. H. Rhodes, G. Agranov, C. Hong, U. Boettiger, R. Mauritzson, J. Ladd, I. Karasev, J. McKee, E. Jenkins, and W. Quinlin, "CMOS imager technology shrinks and image performance," in *IEEE Workshop on Microelectronics and Electron Devices* (IEEE, 2004), pp. 7–18.
6. P. B. Catrysse and B. A. Wandell, "Roadmap for CMOS image sensors: Moore meets Planck and Sommerfeld," Proc. SPIE **5678**, 1–13 (2005).
7. P. B. Catrysse and B. A. Wandell, "Integrated color pixels in 0.18 μm complementary metal oxide semiconductor technology," J. Opt. Soc. Am. A **20**, 2293–2306 (2003).
8. P. B. Catrysse, W. J. Suh, S. H. Fan, and M. Peeters, "One-mode model for patterned metal layers inside integrated color pixels," Opt. Lett. **29**, 974–976 (2004).
9. C. C. Fesenmaier, Y. Huo, and P. B. Catrysse, "Optical confinement methods for continued scaling of CMOS image sensor pixels," Opt. Express **16**, 20457–20470 (2008).
10. C. C. Fesenmaier, Y. Huo, and P. B. Catrysse, "Effects of imaging lens *f*-number on sub-2 μm CMOS image sensor pixel performance," Proc. SPIE **7250**, 72500G (2009).
11. Y. J. Huo, C. C. Fesenmaier, and P. B. Catrysse, "Microlens performance limits in sub-2 μm pixel CMOS image sensors," Opt. Express **18**, 5861–5872 (2010).
12. R. Singh and V. Mittal, "Mercury cadmium telluride photoconductive long wave infrared linear array detectors," Def. Sci. J. **53**, 281–324 (2003).
13. A. Rogalski, J. Antoszewski, and L. J. Faraone, "Third-generation infrared photodetector arrays," Appl. Phys. **105**, 091101 (2009).
14. P. B. Catrysse and B. A. Wandell, "Optical efficiency of image sensor pixels," J. Opt. Soc. Am. A **19**, 1610–1620 (2002).
15. G. Veronis and S. Fan, "Overview of simulation techniques for plasmonic devices," in *Surface Plasmon Nanophotonics*, M. L. Brongersma and P. Kik, eds. (Springer, 2007), Vol. **131**, p. 169.
16. W. Shin and S. Fan, "Choice of the perfectly matched layer boundary condition for frequency-domain Maxwell's equations solvers," J. Comput. Phys. **231**, 3406–3431 (2012).
17. E. D. Palik and G. Ghosh, *Handbook of Optical Constants of Solids* (Academic, 1985).
18. M. Born and E. Wolf, *Principles of Optics: Electromagnetic Theory of Propagation, Interference and Diffraction of Light*, 6th ed. (corrected) (Pergamon, 1980).